

Flexoelectricity-driven giant polarization in (Bi, Na)TiO₃-based ferroelectric thin films

Received: 17 February 2025

Accepted: 16 October 2025

Published online: 26 November 2025

 Check for updates

Yunlong Sun  ¹, Ranming Niu  ^{2,3}, Zizheng Song ^{4,5}, Shiyu Tang ⁶, Huizhong Wang ¹, Xun Geng ⁷, Ji Zhang  ^{1,8}, Jack Yang  ^{1,8}, Claudio Cazorla  ⁹, Changqing Guo ⁶, Shery L. Y. Chang ¹, Xiaojie Lou  ¹⁰, Houbing Huang  ⁶ , Zibin Chen  ^{4,5} , Shujun Zhang  ¹¹ & Danyang Wang  ¹ 

This study demonstrates the use of oxygen vacancy-induced planar defects to significantly enhance electrical polarization through a local flexoelectric effect. By introducing an appropriate level of aliovalent dopants, numerous local planar defects are induced in (Bi_{0.5}, Na_{0.5})TiO₃-based thin films. These defects, identified as oxygen-deficient structures through direct visualization of oxygen atoms and oxygen vacancies using integrated differential phase-contrast microscopy, result in the formation of head-to-head domain structures. Geometric phase analysis confirms that these structures exhibit a substantial local strain gradient of up to 10⁹ m⁻¹, contributing significantly to the flexoelectric polarization. Consequently, a giant maximum polarization (P_m) of 161 $\mu\text{C cm}^{-2}$ under 750 kV cm⁻¹ and a remanent polarization $P_r = 115 \mu\text{C cm}^{-2}$ along with a coercive field of 250 kV cm⁻¹ are achieved, allowing these (Bi_{0.5}, Na_{0.5})TiO₃-based thin films to be used in low-power electronic applications. Crucially, the P_m and P_r of the thin films can be sustained at 133 and 98 $\mu\text{C cm}^{-2}$, respectively, at 230 °C. Additionally, they exhibit exceptional high-temperature fatigue endurance, with P_m and P_r demonstrating a negligible reduction of less than 9% after 10⁷ cycles under 750 kV cm⁻¹ at 230 °C. These values surpass those previously reported for oxide perovskite thin films at elevated temperatures, demonstrating potential applications of our thin films in high-temperature environments. Our findings offer promising avenues for advancing the application fields of ferroelectric thin films.

Large polarization is consistently pursued and anticipated in ferroelectric thin films due to its ability to facilitate superior energy storage capacity, improved electro-mechanical coupling efficiency, and elevated dielectric constants¹, which significantly impacts the functional properties and performance of various devices, including solid-state cooling systems, electrostatic energy storage units, non-volatile random-access memory (FeRAM), and ultrasound medical imaging technologies². In conventional thin films possessing perovskite structures, enhanced polarization is typically attained through employing highly lattice-mismatched substrates. For example, BiFeO₃ (BFO) thin

films grown on LaAlO₃ substrates experience significant compressive epitaxial strain (~4.5%), stabilizing a maximum polarization of ~130 $\mu\text{C cm}^{-2}$ ³⁻⁵. Another viable route to improve polarization involves utilizing interphase strain in nanocomposite-like films to generate super tetragonal (super-T) structures. A super-tetragonal phase is used to describe the unique lattice structure in perovskite oxide thin films that exhibits a markedly large c/a ratio, e.g., 1.10-1.25⁶⁻⁸, often resulting in an enhanced polarization. Such super-T structures arise from mismatches in c -lattice parameter between the thin film material and a secondary phase, such as PbO in PbTiO₃ thin films⁶, BaO in BaTiO₃ thin

A full list of affiliations appears at the end of the paper.  e-mail: hbhuang@bit.edu.cn; zi-bin.chen@polyu.edu.hk; dy.wang@unsw.edu.au

films⁷, and β - Bi_2O_3 in $(\text{Bi}_{0.5}\text{Na}_{0.5})\text{TiO}_3$ -based thin films⁸, precipitated due to local chemical inhomogeneities, leading to unusually large polarizations exceeding $100 \mu\text{C cm}^{-2}$.

Despite the efficacy of these established methodologies, their limitations are evident. The improvement in polarization achieved through compressive strain from the substrate is finite. As the thickness of thin films increases, the strain imposed by the substrate diminishes, causing the films to gradually revert to their bulk lattice parameters and properties^{3-5,9}. Similarly, when leveraging interphase strain from a secondary phase, a high coercive field (E_c), typically exceeding 2000 kV cm^{-1} , is often necessary for switching domains. The requirement for such substantial power consumption to achieve heightened polarization raises serious concerns regarding Joule heating and catastrophic dielectric breakdown^{6,7}, which are particularly severe at elevated temperatures and also pose challenges for the supporting insulation system, potentially restricting their use in highly integrated miniaturized devices. Balancing the operating field and polarization, i.e., achieving both a low coercive field and large polarization simultaneously, remains a challenge for ferroelectric thin films, especially in the development of beyond-complementary metal oxide semiconductor devices.

In this work, we demonstrate the feasibility of enhancing polarization in relatively thick films under a low driving field by leveraging the flexoelectric effect. The incorporation of Fe cations into $0.94(\text{Bi}_{0.5}, \text{Na}_{0.5})\text{TiO}_3\text{-}0.06\text{BaTiO}_3$ (BNBT) thin films facilitate the creation of oxygen vacancies, which accumulate in tail-to-tail (T-T) domain walls as charged defects by creating oxygen-deficient superstructures (planar defects). Between the T-T domain walls, head-to-head (H-H) domain walls emerge, generating a giant local strain gradient that can reach a level of up to 10^9 m^{-1} , contributing significantly to flexoelectric polarization. Consequently, we achieve a giant maximum polarization (\mathbf{P}_m)

of $161 \mu\text{C cm}^{-2}$ under 750 kV cm^{-1} and a remanent polarization $\mathbf{P}_r = 115 \mu\text{C cm}^{-2}$ along with a coercive field of 250 kV cm^{-1} , demonstrating superior polarization compared with previously reported lead-free ferroelectrics under a comparable electric field.

Results

Room-temperature ferroelectric hysteresis (P - E) loops of Fe-doped BNBT (Fe-BNBT) thin films under selected electric fields are presented in Fig. 1a. The maximum polarization values observed are 161, 118, and $95 \mu\text{C cm}^{-2}$ for thin films grown on [001], [110], and [111]-oriented SrTiO_3 substrates, respectively, consistent with the empirical relationship of polarization along different crystallographic orientations of a typical tetragonal lattice¹⁰, unequivocally demonstrating the tetragonal structure of our Fe-BNBT thin films. To quantify the \mathbf{P}_r , the remanent P - E loops were measured under 750 kV cm^{-1} , as illustrated in Fig. 1b. A significant \mathbf{P}_r of $115 \mu\text{C cm}^{-2}$ was achieved for the [001]-oriented Fe-BNBT thin films. Figure 1c shows the out-of-plane X-ray diffraction (XRD) θ - 2θ scan results of Fe-BNBT thin films, indicating that the growth orientation of the films aligns with their respective substrates. Given the tetragonal structure of our Fe-BNBT thin films and their optimal ferroelectric properties when grown on a [001]-oriented substrate, we will concentrate on [001]-oriented films to understand the origin of the large polarization. The XRD reciprocal space map (XRD-RSM) measurements were performed to ascertain the in-plane lattice parameters of Fe-BNBT thin films. As illustrated in Fig. 1(d), diffraction spots referring to LSMO, STO, and Fe-BNBT layers are evident. The identical Q_x values of these diffraction spots in the RSM of Fe-BTBT suggest that both Fe-BNBT and LSMO layers are fully strained on the STO substrate. The lattice parameters a and c are calculated as 3.905 and 3.919 \AA , respectively. Importantly, neither super-T having elongated c lattice parameter were observed nor was

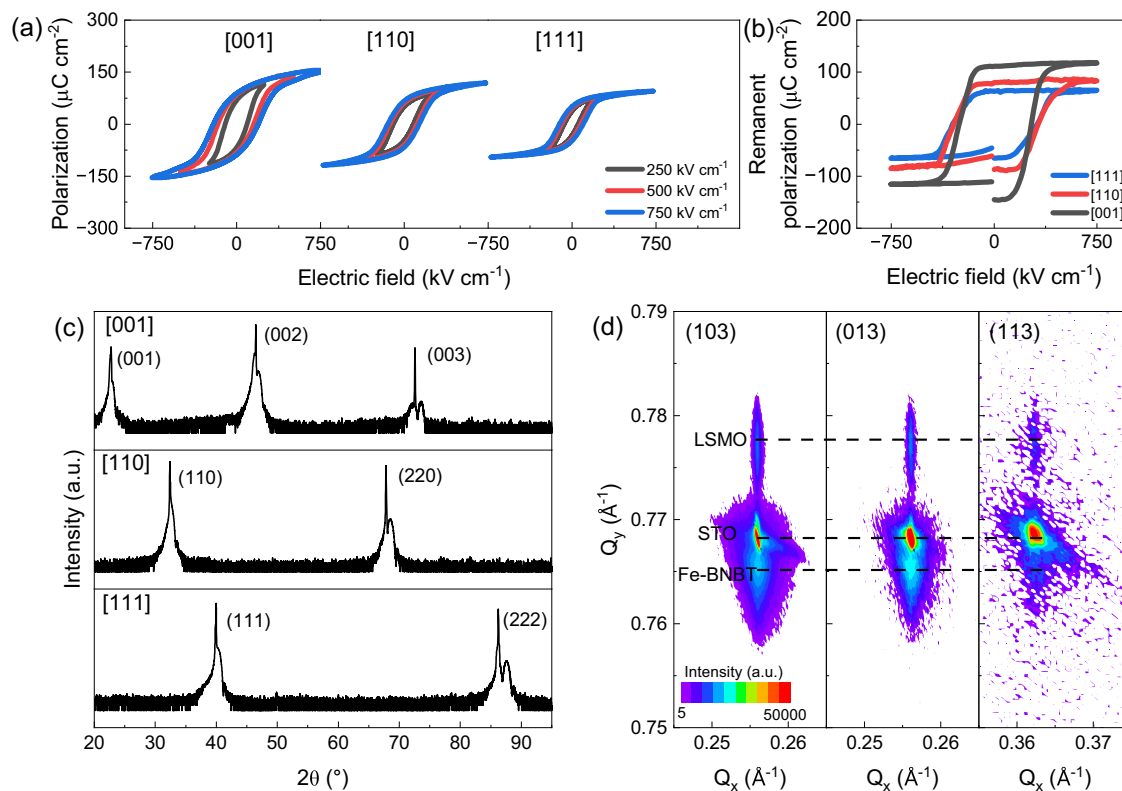


Fig. 1 | Structural and ferroelectric characteristics of Fe-BNBT thin films. **a** The room-temperature P - E loops of [001], [110], and [111]-oriented Fe-BNBT thin films under selected electric fields. **b** The room-temperature remanent P - E loops of [001], [110], and [111]-oriented Fe-BNBT thin films under 750 kV cm^{-1} . **c** XRD θ - 2θ scan patterns of [001], [110], and [111]-oriented Fe-BNBT thin films. **d** XRD-RSM patterns around (103), (013), and (113) reflections of [001]-oriented Fe-BNBT thin films.

scan patterns of [001], [110], and [111]-oriented Fe-BNBT thin films. **d** XRD-RSM patterns around (103), (013), and (113) reflections of [001]-oriented Fe-BNBT thin films.

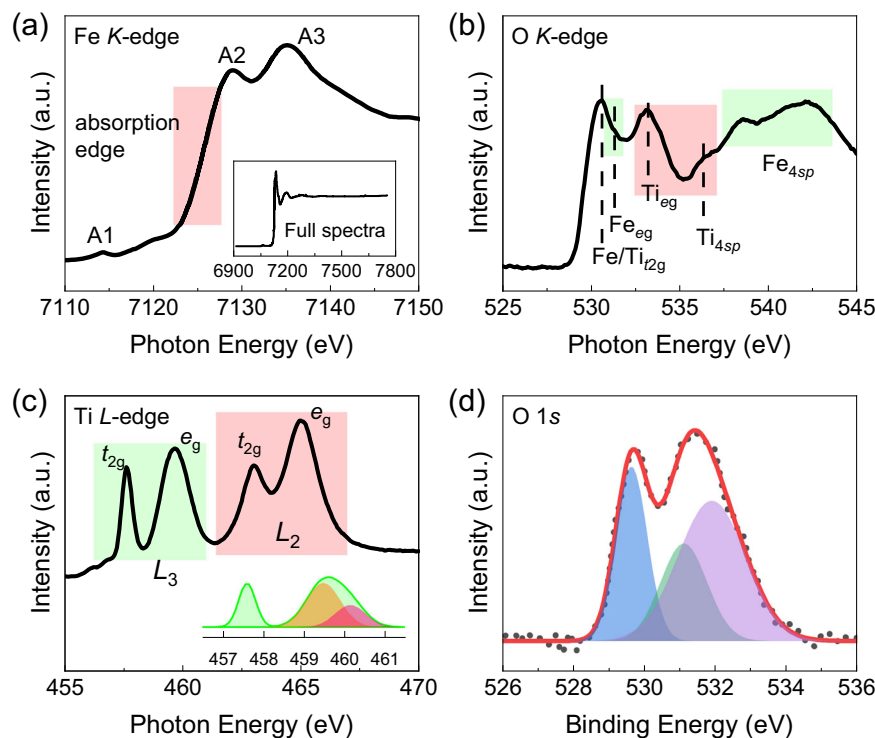


Fig. 2 | X-ray absorption and photoelectron spectra of Fe-BNBT thin films. The a Fe *K*-edge, b O *K*-edge, and c Ti *L*-edge XAS spectra of Fe-BNBT thin films acquired in total fluorescence yield (TFY) mode. The inset in (a) refers to the full spectra of Fe *K*-edge. The inset in (c) is the result of peak fitting of the L_3 eg peak of Fe-BNBT thin films. The configuration interaction cluster model calculation is a computational technique used in quantum chemistry and solid-state physics to study the

electronic structure of atomic systems, which is particularly valuable in systems with strong electron correlation. d XPS spectra of the O 1s electronic level for Fe-BNBT thin films. Blue, green, and purple peak is ascribed to the lattice oxygen, lattice oxygen connected with the lower valence cation after vacancy creation, and the adsorbed surface water and/or hydroxyl molecules, respectively.

substantial in-plane strain (-0.5%) detected in the XRD and RSM results, suggesting the presence of some other potential contributions to the observed large polarization.

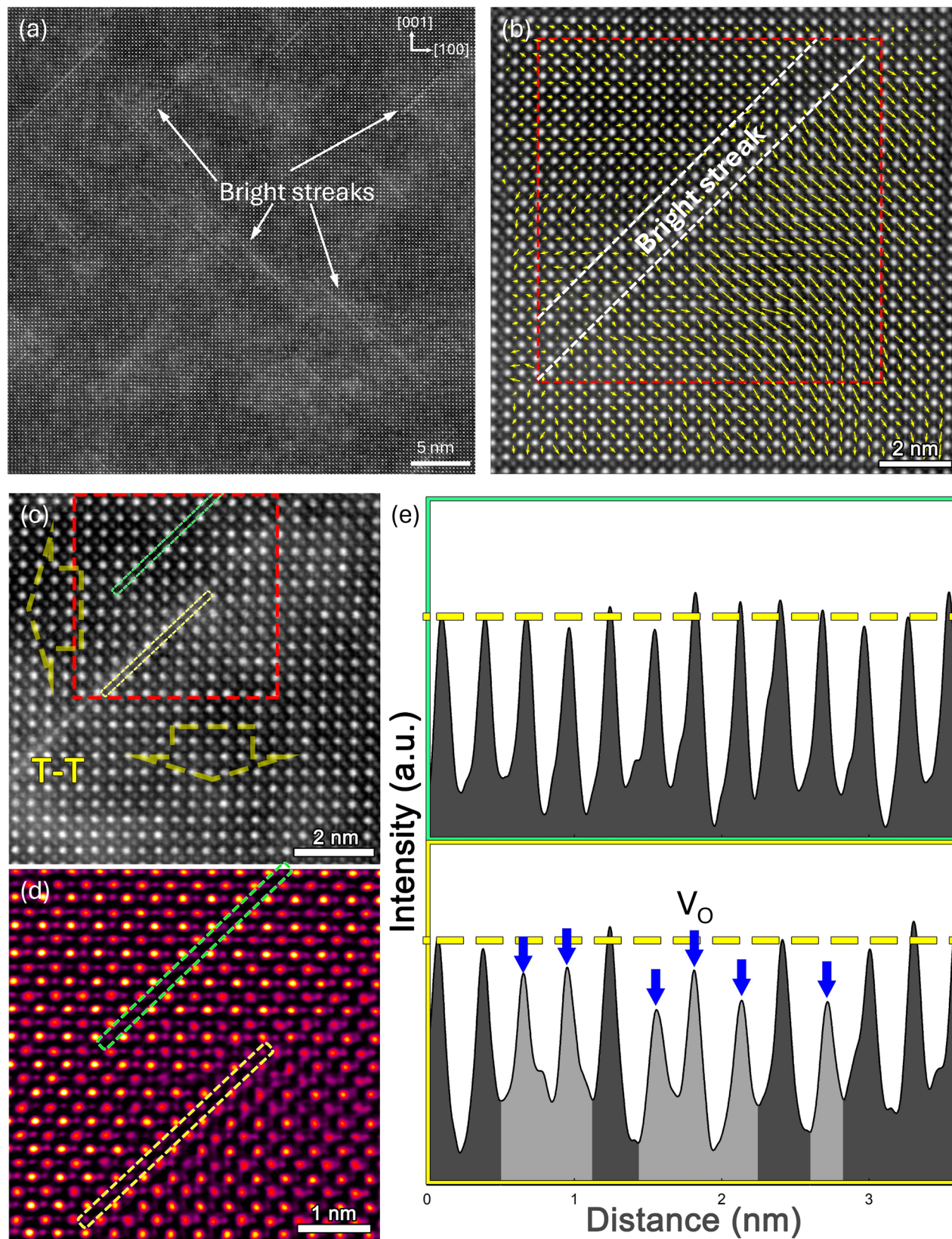
Orbital hybridization plays an essential role for the emergence of ferroelectricity in the thin films of complex oxides¹¹. To understand the electronic structure and orbital hybridization, Fe-BNBT thin films were examined using X-ray absorption spectroscopy (XAS). Figure 2(a) illustrates the Fe *K*-edge XAS spectra of Fe-BNBT thin films. The absorption edge energy is determined to be 7126.14 eV, consistent with that of Fe_2O_3 , indicating the valent state of Fe is 3+¹². Additionally, the pre-edge peak A1 and post-edge A2 and A3 are also observed, attributed to the electric quadrupole-forbidden transition from the O 1s level to Fe 3d, O 2p band to Fe 3d orbit, and O 1s to Fe 4p dipole-allowed transition, respectively. This confirms that the Fe^{3+} cations enter into the B sites by replacing Ti^{4+} ¹³. Fig. 2(b) illustrates the O *K*-edge XAS spectra of Fe-BNBT thin films, revealing signals originating from the hybridization of the O 2p and unoccupied Ti/Fe 3d orbitals. The diminished peak intensity ratios of e_g and t_{2g} signals (<1) imply a weakening of the Ti-O and Fe-O bonds in the hybridization of O 2p and Ti/Fe 3d orbitals, suggesting the possible formation of oxygen vacancies within the Fe-BNBT thin films¹⁴.

The Ti *L*-edge XAS spectra of Fe-BNBT are illustrated in Fig. 2c to investigate the symmetry of the TiO_6 octahedron. L_3 and L_2 edges are generated by the spin-orbit interaction in the spectra, and each edge contains t_{2g} and e_g peaks. The L_3 eg state is oriented toward ligand anions, making it more responsive to deviations from the Ti octahedral symmetry¹⁵. As shown in the inset of Fig. 2(c), the observed splitting of L_3 eg is associated with the non-centrosymmetric TiO_6 octahedron, affirming the tetragonal structures of Fe-BNBT films¹⁶. Notably, the relatively higher intensity of the peak localized at low photon energy (yellow) compared to the high-photon energy peak (pink) is connected

with the localized character of the e_g states, demonstrating the existence of defective structures in Fe-doped BNBT thin films¹⁶. These distortions are most likely induced by oxygen vacancies and associated planar defects, stemming from the replacement of Ti by Fe cations. Such structural and chemical disorder reduces the local symmetry and modifies the crystal field environment, leading to orbital energy shifts and increased localization of the e_g electrons¹⁶. Moreover, based on the configuration interaction cluster model calculation, an increased ratio of the peak intensity of the e_g and t_{2g} peaks ($I_{eg/t2g}$) usually indicates enhanced tetragonal distortion¹⁷. The $I_{eg/t2g}$ value for Fe-BNBT films is calculated as 1.1, suggesting a high level of local strain in Fe-BNBT films¹⁶.

X-ray Photoelectron Spectroscopy (XPS) was employed to estimate the level of oxygen vacancy in Fe-BNBT thin films. As shown in Fig. 2(d), the deconvolution of the O 1s peak suggests the presence of lattice oxygen O_L (blue peak), the lattice oxygen connected with the lower valence cation after vacancy creation O_V (green peak), and adsorbed surface water and/or hydroxyl molecules O_C (purple peak)^{18,19}. The observation of O_V XPS peak echoes a strong correlation between the defective structure observed via XAS and the presence of oxygen vacancies.

To clarify the critical role of oxygen vacancies in producing large polarization in our Fe-BNBT thin films, high-angle annular dark-field (HAADF) scanning transmission electron microscopy (STEM) measurements were conducted. The thickness of the films was confirmed to be ~550 nm through low-magnification HAADF-STEM images (Supplementary Fig. 1). Notably, numerous two-dimensional and oriented segments along [101] and [-101] (referred to as bright streaks) are observed in the Fe-BNBT thin films (Fig. 3(a)). Polarization mapping was performed to examine the impact of bright streaks on the domain structures of Fe-BNBT thin films. The length and direction of the



arrows represent the strength and orientation of the polarization, respectively. Significantly, T-T domain walls appear near the bright streak regions in our Fe-BNBT thin films (Fig. 3 (b)). Density functional theory (DFT) calculations indicate that the aggregation of oxygen vacancies can give rise to charged T-T domain walls²⁰. The formation of oxygen vacancies in Fe-doped BNBT can be described using the defect

chemistry notation: $Fe_2O_3 \rightarrow 2^{Ti}O_2 2Fe^{+}_{Ti} + V_O^{\bullet} + 3O_O^X$. To further investigate the structural features of these bright streaks, integrated differential phase-contrast (iDPC) imaging was employed. This advanced imaging technique can enhance the image contrast of weakly absorbing, low-atomic-number elements, enabling the simultaneous determination of heavy and light element positions²¹. The iDPC-STEM

Fig. 3 | Atomic-resolution STEM analysis revealing T-T domain walls and associated structural features in Fe-BNBT thin films. **a** A HAADF STEM images of Fe-BNBT thin films, indicating the high density of bright streaks. **b** The polarization map of Fe-BNBT thin films, where the length and direction of the arrows represent the strength and orientation of the polarization, respectively. **c** A magnified view illustrating that the bright streaks act as T-T domain walls in the Fe-BNBT thin films, extracted from the red-dashed square region in **b**. The yellow dashed box indicates the interface between the bright streak and its neighboring unit cell, whereas the

green dashed box denotes a region approximately seven unit cells away from the defect zone. **d** STEM-iDPC image of Fe-BNBT thin films, corresponding to the red-dashed square region in **c**. The yellow dashed box indicates the interface between the bright streak and its neighboring unit cell, whereas the green dashed box denotes a region approximately seven unit cells away from the defect zone.

e Oxygen atom signal intensities from the two regions marked by the yellow and green dashed rectangles in **(c, d)**, demonstrating the contrast difference between the bright streaks and its surrounding areas.

result in Fig. 3(d) effectively distinguishes A/B-site cations and oxygen atoms, revealing that the bright streaks are planar defects enriched with oxygen vacancies, as delineated by the yellow dotted rectangle. To provide a more intuitive representation of the oxygen vacancies within the bright streaks, the intensity of oxygen atom signals from two regions—denoted by green and yellow dotted rectangles—was analyzed (Fig. 3(e)). Compared to the surrounding areas (green), the bright streaks (yellow) exhibit a significantly lower contrast, as indicated by blue arrows, underscoring the presence of a nonstoichiometric Fe-BNBT lattice in the vicinity of the streaks. These findings provide compelling evidence that oxygen vacancies are localized within the bright streaks, serving as charged defects, contributing to the formation of T-T domain walls in our Fe-BNBT thin films.

We conducted first-principles calculations based on density functional theory (DFT, Experimental Section) to gain further insight into the onset of the nonstoichiometry (planar defects) in Fe-BNBT. Given that XRD and XAS results confirm the tetragonal structure of our BNBT thin films, we adopted a tetragonal phase with a space group of P4/mmb²² for the DFT calculation, as illustrated in Supplementary Fig. 2a. To investigate the structural stability of BNBT, the formation energy of BNBT unit cells with various dopants, i.e., Mn and Fe cations, were simulated. The formation energies of BNBT unit cells with oxygen vacancies and without oxygen vacancies are given in Supplementary Fig. 2(b). In comparison to Mn-doped BNBT, whose formation energy of the pristine structure is situated between the BNBT unit cells exhibiting oxygen vacancy-related distortions, defect-free Fe-doped BNBT has the highest formation energy. This indicates that the creation of oxygen vacancy favors a more stable Fe-BNBT structure, which is in line with our experimental observations.

Given the high density of planar defects in the films, an intriguing question arises regarding how the domain structures transform between two adjacent T-T domain walls. To address this question, we conducted polarization mapping over a large area (55×20 nm²), as shown in Fig. 4a. Interestingly, H-H domains were found to form between adjacent pairs of bright streaks. The polarization mapping reveals enhanced polarization strength near the H-H domain walls. Figure 4(c) depicts the enlarged polarization maps of Fe-BNBT thin films, with areas 1 and 2 corresponding to the regions outlined by red dashed boxes in Fig. 4(a), which highlights distinct disparities. In area 1, BNBT unit cells adjacent to H-H domain walls exhibit substantial polarization (represented by longer arrows), with polarization diminishing progressively in unit cells further from the domain walls. Conversely, the polarization in area 2, which features H-T domain structures, appears weak and uniformly distributed. To analyze the mechanism behind the enhanced polarization observed near H-H domain walls, as opposed to areas with T-T and H-T domain structures, geometric phase analysis (GPA) is utilized to map the strain distribution in Fe-BNBT thin films, using the strain level of stoichiometric BNBT unit cells (area 2) as a reference. Figure 4(b) displays the strain mapping results of Fe-BNBT thin films generated by GPA. In contrast to the negligible strain levels found in areas with T-T and H-T domain structures, a significant local strain of ~10% is observed near the H-H domain walls, which is believed to be responsible for the increased polarization observed in area 1. Moreover, a strain gradient oriented along the white arrow is also obtained. Figure 4(d) illustrates the level of strain and strain gradient as a function of distance along the direction of the

white arrow in Fig. 4(b). Notably, Fe-BNBT thin films exhibit a substantial local strain gradient, reaching up to 10⁹ m⁻¹.

Strain gradients inherently give rise to flexoelectric polarization. A previous study has reported that a large strain gradient on the order of 10⁶ m⁻¹ was found in LaFeO₃ thin films grown on (001) LaAlO₃ single crystal substrates²³, giving rise to a flexoelectric polarization of 9.27 μC cm⁻². The strain-gradient-induced electrical polarization (flexoelectric polarization, P_F) can be determined by²⁴:

$$P_F = \mu_{ijkl} \frac{\partial \epsilon_{ij}}{\partial x_k} \quad (1)$$

where μ_{ijkl} is the fourth-rank flexoelectric coefficient and $\partial \epsilon_{ij} / \partial x_k$ is the strain gradient. Thus, the polarization for ferroelectrics involving flexoelectric effect can be expressed by:

$$P = P_D + P_F = \chi_{ij} E_j + \mu_{ijkl} \frac{\partial \epsilon_{ij}}{\partial x_k} \quad (2)$$

where χ_{ij} is the dielectric susceptibility of the ferroelectrics, E_j the applied electric field. $P_D = \chi_{ij} E_j$ describes the polarization stemming from the dielectric response. To assess the contribution of flexoelectricity to the observed polarization of Fe-BNBT thin films, the determination of the flexoelectric coefficient is necessary. Unfortunately, no commercially available techniques currently exist that enable a standardized process for measuring the flexoelectric coefficient in thin films with compelling reliability and accuracy²⁴. Previous reports revealed that the flexoelectric coefficient of perovskite-structured single crystals was on the order of magnitude of 10¹ to 10¹ nC m⁻¹, e.g., $|\mu_{11}|$, $|\mu_{12}|$, and $|\mu_{44}|$ are 0.15, 5.5, and 1.9 nC m⁻¹ for BaTiO₃ single crystal and 0.2, 7 and 5.8 nC m⁻¹ for SrTiO₃ single crystal, respectively²⁴. By incorporating this range of flexoelectric coefficient into Equation (1), the flexoelectric polarization of our Fe-BNBT thin films can be up to 100 μC cm⁻². We also computed the polarization of typical BNBT with a tetragonal structure ($c/a = 1.004$). The calculated electrical polarization is 60.88 μC cm⁻², which closely aligns with our experimental findings, i.e., 160.88 (60.88 μC cm⁻² from the dielectric response + 100 μC cm⁻² from the flexoelectric effect) vs 161 μC cm⁻². Considering the high density of such local “planar defects” and the associated H-H domain structures in Fe-BNBT thin films, the exceptionally high local strain gradient is believed to play a pivotal role in generating the overall giant polarization.

The phase-field simulation was employed to verify the contribution of the flexoelectric effect to the improved polarization. Details of the phase-field simulations are provided in the Experimental Section. A typical ferroelectric with a tetragonal structure was established as the initial state in a BNBT single crystal. Bound charges were introduced to simulate the oxygen vacancies concentrated at bright streaks (planar defects). Compared to typical BNBT with H-T domain configurations (Fig. 5a, g), T-T domain walls are created upon the introduction of local charges, with H-H domain structures forming between adjacent T-T domain walls (Fig. 5b, h), consistent with observations from STEM. Additionally, strain mapping analysis, presented in Fig. 5c, d, revealed elevated strain levels at the H-H domain walls, while typical BNBT exhibited relatively low and uniformly distributed strain, confirming the presence of strain gradient in films. This finding aligns with the

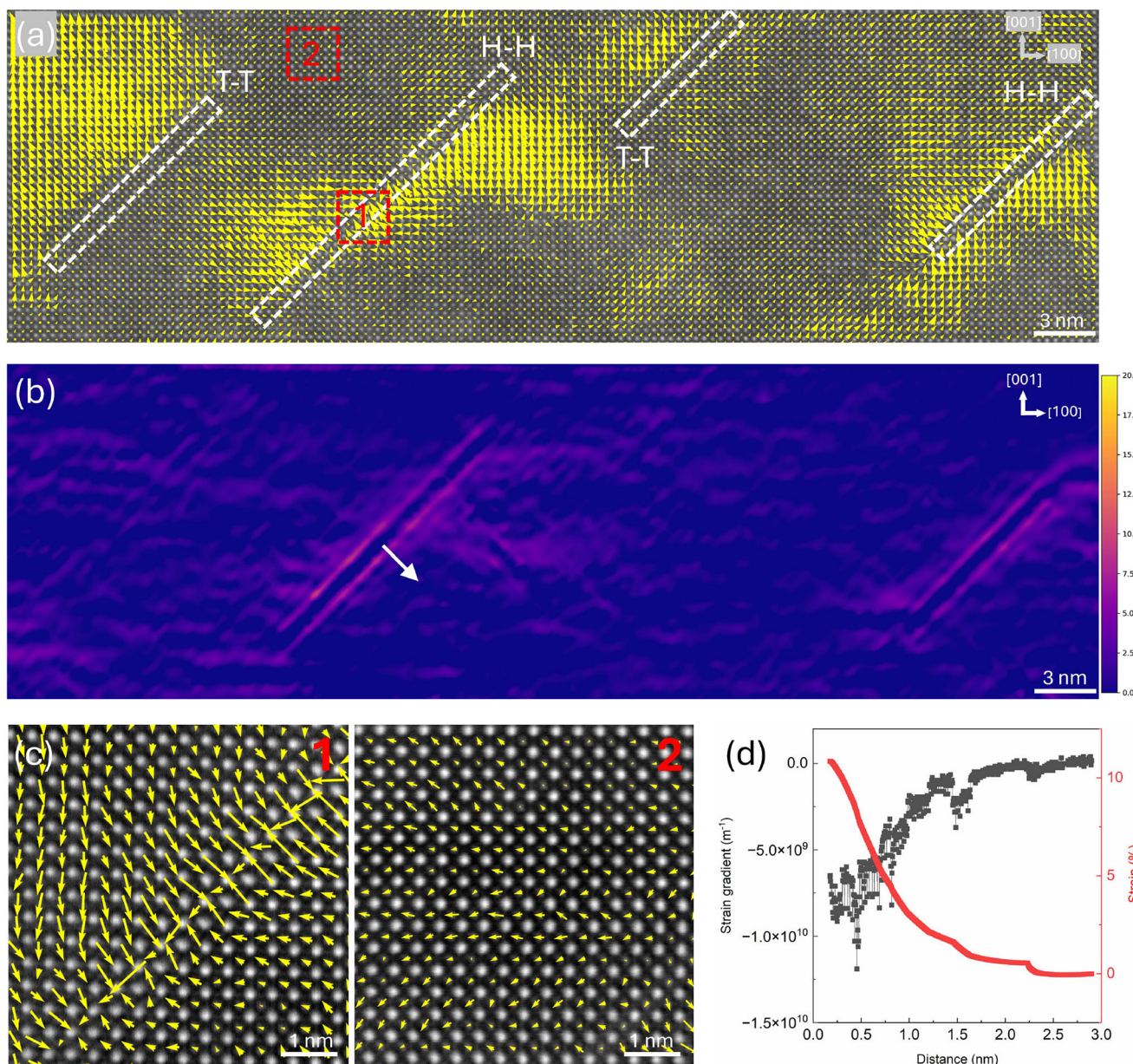


Fig. 4 | Polarization and strain distribution in Fe-BNBT thin films revealed by STEM-GPA analysis. **a** The polarization maps of Fe-BNBT thin films. **b** The strain maps of Fe-BNBT thin films generated by GPA. **c** The enlarged polarization maps of

Fe-BNBT thin films, with areas 1 and 2 corresponding to the regions outlined by red dashed boxes in **a**. **d** The level of strain and corresponding strain gradient of Fe-BNBT thin films as a function of distance along the white arrow in **b**.

simulated P - E loops, where the bound charge-modified Fe-BNBT demonstrates enhanced \mathbf{P}_m and \mathbf{P}_r , compared to the typical BNBT, while their \mathbf{E}_c remains comparable (Fig. 5e, f). This supports the role of the flexoelectric effect in producing the substantial polarization observed in our BNBT thin films. Furthermore, the T-T and H-H domains exhibit remarkable switchable behavior under electric field stimulation. These domains can be reoriented in response to the applied electric field, and upon the removal of the field, only a small fraction of the domains revert to their initial configuration, while the majority maintain their alignment (Supplementary Fig. 3). This behavior accounts for the exceptional \mathbf{P}_r observed in the Fe-BNBT thin film.

To assess the thermal stability of the ferroelectricity in Fe-BNBT thin films, temperature-dependent P - E loops were measured, as illustrated in Fig. 6a–c. Remarkably, the \mathbf{P}_m and \mathbf{P}_r of Fe-BNBT thin films can be maintained at 133 and 98 $\mu\text{C cm}^{-2}$ at 230 °C, respectively, indicating that temperature has minimal impact on the strength of the

flexoelectric effect. To the best of our knowledge, these values surpass those previously reported for oxide perovskite thin films at elevated temperatures, highlighting their potential for applications in high-temperature environments, particularly in advanced FeRAM systems for aerospace and defense technologies. A charging and discharging frequency of 50 kHz was employed to conduct the fatigue measurement of P - E loops under an AC electric field of 750 kV cm^{-1} , both at room temperature and at 230 °C. Figure 6d, e present the P - E loops of 550 nm-thick Fe-BNBT thin films with respect to the electric field cycles, indicating the variation in \mathbf{P}_m and \mathbf{P}_r . At room temperature, a reduction in \mathbf{P}_m and \mathbf{P}_r is found to be 14% and 23%, respectively, compared to the respective values before cycling, indicating a reasonably good endurance to cycling stress. Notably, Fe-BNBT thin films exhibited exceptional fatigue endurance at 230 °C, with \mathbf{P}_m and \mathbf{P}_r showing only marginal decreases to 122 and 90 $\mu\text{C cm}^{-2}$, respectively, representing less than 9% variation. This highlights the extraordinary

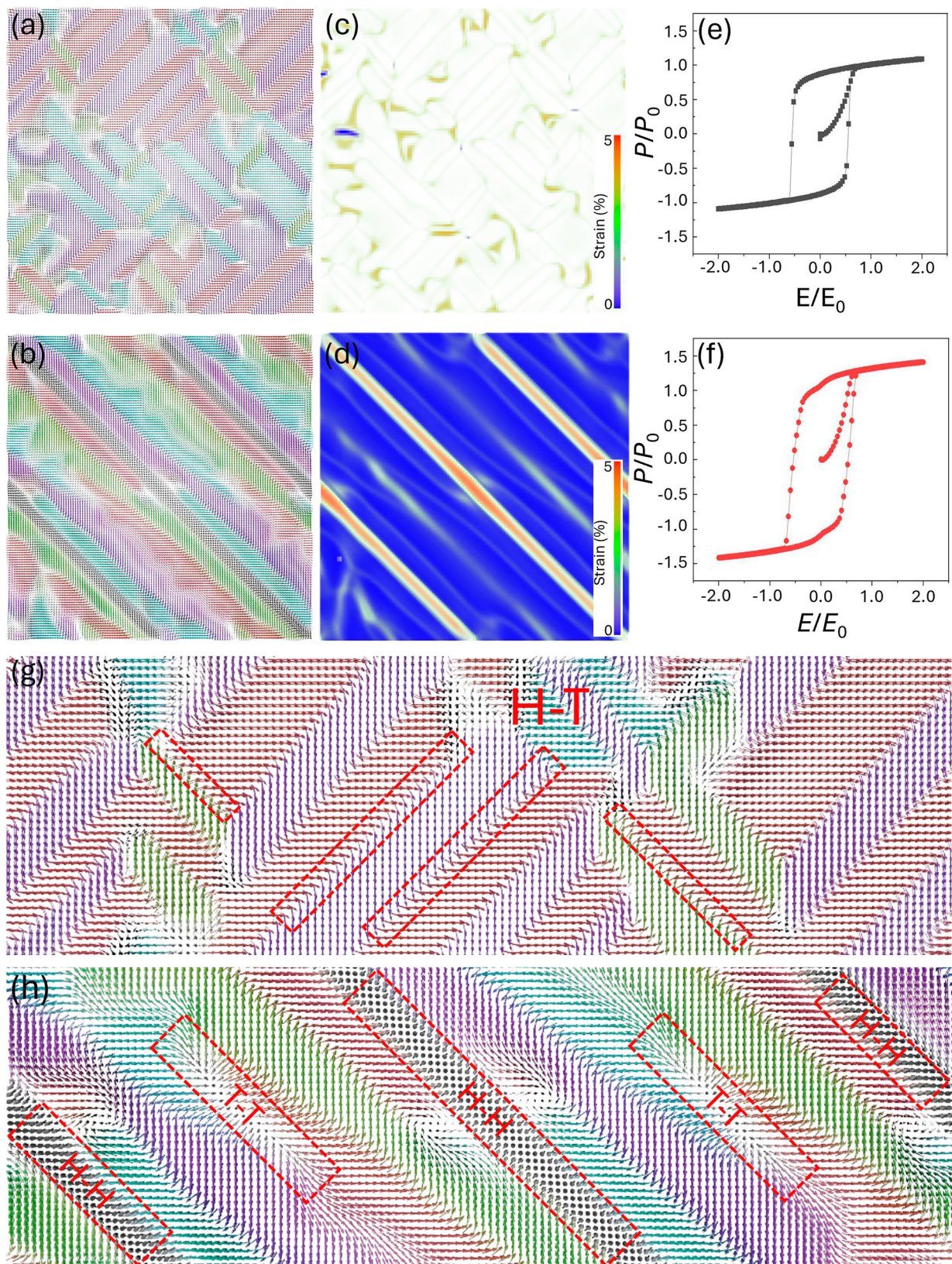


Fig. 5 | Phase-field simulation results of polarization, strain, and P - E behavior in BNBT thin films with and without planar defects. Phase-field simulations display polarization mapping in **a** the initial BNBT and **b** the bound charge-modified BNBT. Strain mapping results of **c** initial BNBT and **d** bound charge-modified BNBT.

The simulated P - E loops for **e** initial BNBT and **f** bound charge-modified BNBT. Enlarged views of the polarization mapping for **g** initial BNBT and **h** bound charge-modified BNBT, which are derived from **a**, **b**, respectively.

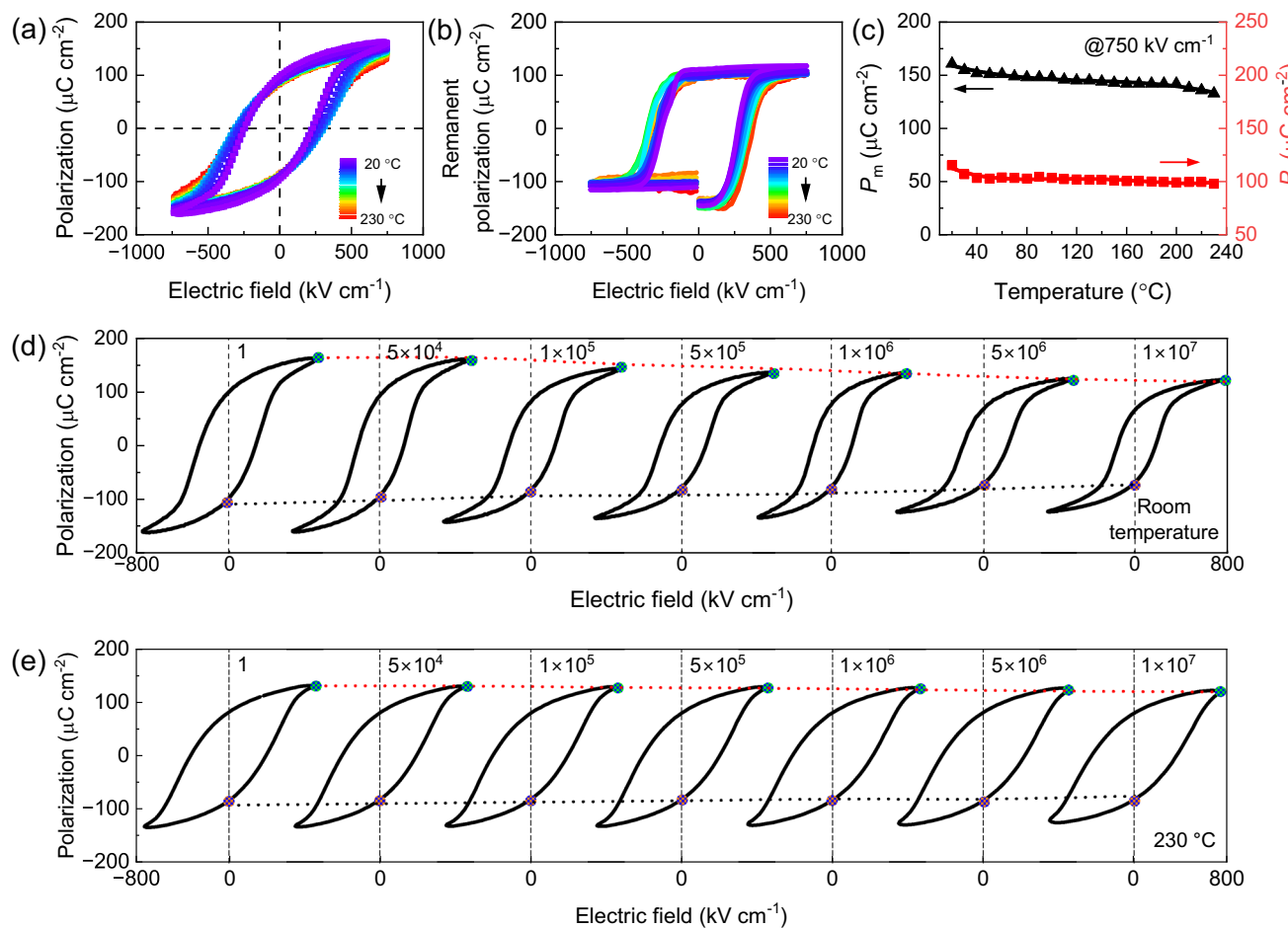


Fig. 6 | Evolution of polarization and P - E loops in Fe-BNBT thin films with temperature and cyclic electric loading. **a** The temperature-dependent P - E loops of Fe-BNBT thin films under 750 kV cm^{-1} . **b** The temperature-dependent remanent P - E loops of Fe-BNBT thin films under 750 kV cm^{-1} . **c** The maximum polarization and the remanent polarization of Fe-BNBT thin films under selected electric fields as a function of temperature. **d, e** The P - E loops of Fe-BNBT thin films were evaluated at a frequency of 50 kHz under an AC electric field of 750 kV cm^{-1} at room temperature and at $230 \text{ }^\circ\text{C}$ during fatigue testing, with the number of electric cycles extending up to 10^7 , respectively.

as a function of temperature. **d, e** The P - E loops of Fe-BNBT thin films were evaluated at a frequency of 50 kHz under an AC electric field of 750 kV cm^{-1} at room temperature and at $230 \text{ }^\circ\text{C}$ during fatigue testing, with the number of electric cycles extending up to 10^7 , respectively.

thermal stability of the ferroelectric properties in the flexoelectricity-enhanced Fe-BNBT thin film, emphasizing their suitability for high-temperature applications. The superior fatigue endurance at elevated temperatures, compared to room temperature, may be attributed to the reduced impact of the pinning effect at higher temperatures²⁵, which further reinforces the feasibility of Fe-BNBT thin films for deployment in extreme thermal environments.

Table 1 compares the P_m , P_r , and E_c of the best-performing ferroelectric thin films to date. BFO-based thin films exhibit relatively low E_c and can simultaneously maintain high values of P_m and P_r , however, polarizations of the biaxial strain-modified BFO thin films are prone to temperature, as even a slight increase in temperature can lead to substantial electric leakage, severely degrading their performance at elevated temperatures. Likewise, although incredibly large remanent polarization of 100 and $236 \mu\text{C cm}^{-2}$ were reported in BaTiO_3 and PbTiO_3 thin films, respectively, the intensely high coercive field, i.e., $>2000 \text{ kV cm}^{-1}$, trigger grave concerns over electric breakdown, rapid degradation, and Joule heating, which greatly restricts their practical applications. In contrast, our Fe BNBT thin films demonstrate excellent thermal stability, and exhibit a significantly lower E_c of 250 kV cm^{-1} and a giant P_r of $115 \mu\text{C cm}^{-2}$. This performance surpasses that of the majority of state-of-the-art ferroelectrics under a comparable strength of driving electric fields ($E_{\max} = 750 \text{ kV cm}^{-1}$).

Discussion

To confirm the reproducibility of the giant polarization, we fabricated multiple Fe-doped BNBT thin films under optimized processing conditions. The P - E loops of five Fe-doped BNBT thin films are presented in Supplementary Fig. 5. The highly consistent ferroelectric properties observed across all samples clearly demonstrate the excellent reproducibility of the giant polarization in our Fe-doped BNBT thin films.

In this work, we achieved a remarkable P_m of $161 \mu\text{C cm}^{-2}$ under 750 kV cm^{-1} and a P_r of $115 \mu\text{C cm}^{-2}$, with an E_c of 250 kV cm^{-1} in Fe-BNBT thin films, primarily attributed to the additional flexoelectric polarization. iDPC imaging confirmed the presence of planar defects (oxygen-deficient BNBT) in the films, leading to the formation of H-H domain configurations. GPA analysis revealed a significant strain gradient of up to 10^9 m^{-1} near these H-H domain walls, generating a flexoelectric polarization up to $100 \mu\text{C cm}^{-2}$, as verified by phase-field simulation and first-principles calculations. Furthermore, the polarization of our Fe-BNBT thin films shows excellent thermal stability, i.e. the P_m and P_r of the thin films are maintained at 133 and $98 \mu\text{C cm}^{-2}$, respectively, even at $230 \text{ }^\circ\text{C}$, highlighting their potential for high-temperature applications. This work demonstrates that harnessing the flexoelectric effect provides an alternative avenue to enhance the polarization of ferroelectric thin films under a relatively low electric field.

Table 1 | Comparison of maximum and remanent polarizations of best-performing ferroelectric thin films to date

Thin films	P _m (μC cm ⁻²)	P _r (μC cm ⁻²)	E _c (kV cm ⁻¹)	E _{max} (kV cm ⁻¹)	Thickness (nm)	Substrates	Ref.
BaTiO ₃	240	100	2000	7500	60	(100) Nb-SrTiO ₃	7
Bi(Fe _{0.93} Mn _{0.05} Zn _{0.02})O ₃	117	117	306	600	670	Pt/TiO ₂ /SiO ₂ /Si(100)	42
BiFeO ₃	115	115	600	1000	160	(001) LaAlO ₃	5
Bi(Fe _{0.95} Mn _{0.05} O ₃)/(Bi _{0.90} La _{0.10})FeO ₃	90	78	168	375	210	(111) SrTiO ₃	43
PbTiO ₃	236	236	4000	7000	129	(100) Nb-SrTiO ₃	6
Pb(Zr _{0.35} Ti _{0.65})O ₃	100	90	140	250	50	(100) SrTiO ₃	44
0.6BiFeO ₃ -0.4PbTiO ₃	80	50	250	820	470	Pt/Si	45
Fe-doped BNBT	161	115	250	750	550	(100) SrTiO ₃	This work

Methods

Experimental

Sample Preparation. Undoped BNBT, along with Mn, La, Sm, Eu, Co, and Fe-doped BNBT ceramic targets for thin film deposition, were prepared by the conventional sintering process. The nominal doping level in our BNBT-based thin films is based on the composition of the ceramic target used for Pulsed Laser Deposition (PLD). 10 mol % excess of Bi₂O₃ was added to the target for compensating the loss of Bi during the sintering and subsequent laser ablation process. BNBT thin films with various thicknesses and Fe contents were grown on La_{0.7}Sr_{0.3}MnO₃ (LSMO)-electroded (001) SrTiO₃ (STO) single crystal substrates (a = 0.3905 nm, cubic) by PLD (PASCAL Combi, Japan). A KrF excimer laser ($\lambda = 248$ nm) with an energy density of ~ 1.45 J cm⁻² and frequency of 5 Hz was adopted for the deposition. The deposition temperature and oxygen partial pressure are 800 °C and 200 mTorr, respectively. Gold top electrodes with a 200 μm diameter were deposited through a shadow mask by a sputter coater (Leica EM ACE600) prior to the electrical measurements.

Characterizations. Temperature-dependent ferroelectric hysteresis (P-E) loops were measured by the Radiant ferroelectric workstation connected with a program-controlled chamber (Linkam, HFS600E-PB4). The room-temperature X-ray diffraction (XRD) patterns and X-ray diffraction reciprocal space mapping (XRD-RSM) were obtained by Smartlab (Rigaku, 9 kW rotating anode thin-film XRD). The XPS measurements were carried out by an X-ray photoelectron spectrometer (Thermo Escalab 250Xi). The orbital hybridization of thin films was evaluated at the Australian Synchrotron and at the Cornell High Energy Synchrotron Source.

Specimens for STEM observations were prepared by focused ion beam (FEI Helios G4 PFIB and Zeiss Auriga dual beam systems). Cross-sectional lamellae were lifted out from the thin films and mounted to copper grids by platinum. Then the lamellae were thinned to the thickness allowing the electron-transparency. HAADF-STEM images were acquired using a HAADF detector in an aberration-corrected FEI-Themis Z operated at 300 kV. The images were obtained with a semi-convergence angle of 17.9 mrad and a collection angle range of 48–200 mrad.

Details of density-functional theory calculations

The formation energy of Mn- and Fe-doped BNBT structures (referred to here as “pristine”) is calculated by substituting a Ti atom in the unit cell with the respective dopant. Starting with this pristine configuration, which has a P4/mmbm symmetry, different configurations are generated by placing a single oxygen vacancy (V_O) in the unit cell, using the configuration tools available in Pymatgen²⁶. Each resulting structure is fully relaxed, allowing atomic positions and lattice parameters to adjust, using the Perdew-Burke-Ernzerhof (PBE)²⁷ functional within the VASP²⁸ code, along with the standard projector augmented-wave (PAW)²⁹ method. A + U correction is applied to properly model

the localized *d*-electronic states of the transition metals. The optimization process proceeds until the residual forces are below 10^4 eV Å⁻¹. An energy cutoff of 520 eV is set for the PAW pseudopotential, and a 4×4×4 Monkhorst-Pack k-point grid is used consistently in all simulations. Spin polarization is activated in all calculations. The formation energy for each optimized structure is then calculated as the difference between its total energy and the stoichiometric sum of the chemical potentials of its constituent elements.

The energetic, structural, and electric polarization properties of lead-free Fe-BNBT thin films were calculated with first-principles methods based on density functional theory (DFT). Due to its relatively small presence and to improve computational affordability, Ba ions were neglected in our system modeling thus we ended up simulating (Bi_{0.5}, Na_{0.5})TiO₃ thin films. The PBE variant of the generalized gradient approximation to DFT²⁷ was used as it is implemented in the VASP package²⁸. The “projector augmented wave” method was employed to represent the ionic cores³⁰, and the following electrons were considered as valence: Bi 6s, 6p, and 5d; Na 3s, 2p, and 2s; Ti 3p, 4s, and 3d; and O 2s and 2p. Wave functions were represented in a plane-wave basis truncated at 650 eV. We used a 40-atom simulation cell in which the usual ferroelectric and anti-ferrodistortive distortions occurring in oxide compounds could be reproduced^{31–34} as well as a chemical disorder in the cation positions. For integrations within the first Brillouin zone, we adopted a Gamma-centered k-point grid of 8x8x8. Geometry relaxations were performed by using a conjugate-gradient algorithm that optimized the volume and shape of the simulation cell as well as the atomic positions. The imposed tolerance on the atomic forces was 0.005 eV Å⁻¹. By using these parameters we obtained total energies that converged to within 0.5 meV per formula unit (f.u.). The electric polarization, *P*, was computed with the Born-effective charges approach^{32,35,36} using the formula:

$$P_i = (1/V) \sum_{jk} Z_{ijk}^* \times u_{jk}$$

where *V* is the volume of the simulation cell, index *j* runs over all the atoms in the simulation cell, indexes *i* and *k* represent Cartesian directions, *u_j* is the displacement vector of the *j*-th atom as referred to as a non-polar reference phase, and *Z_{ijk}* the Born effective charge tensor calculated for a non-polar reference state. The Born effective charge tensor was estimated with first-principles density functional perturbation theory²⁸.

Details of phase-field simulation

The phase-field simulation of BNBT is based on the Ginzburg-Landau-Devonshire theory. By solving the phase-field equation, we can obtain the temporal and spatial evolution of the system’s microscopic structure. In this study, the domain structure uses spontaneous polarization (**P**) as the order parameter. The energy minimization principle is applied to solve both the time-dependent Ginzburg-Landau equation

and the mechanical equilibrium equation³⁷⁻³⁹:

$$\frac{\partial P_i}{\partial t} + L \frac{\delta F}{\delta P_j} = 0$$

$$\frac{\partial(\sigma_{ij}(r, t))}{\partial x} = 0$$

here, L is a kinetic coefficient related to domain wall mobility, F is the total free energy of the system, $\frac{\delta F}{\delta P_j}$ is the thermodynamic driving force for polarization evolution, σ_{ij} is the stress tensor, and r and t represent the spatial coordinate and time, respectively. The total free energy of a bulk system can be defined as follows:

$$F_{total} = F_{bulk}(P) + F_{grad}(P) + F_{elas}(P) + F_{elec}(P, E)$$

where, the total free energy F_{total} is composed of the bulk energy $F_{bulk}(P)$, gradient energy $F_{grad}(P)$, elastic energy $F_{elas}(P)$, and electrical $F_{elec}(P, E)$, where E is the external electric field. The bulk free energy is expressed as a sixth-order polynomial expansion, as follows⁴⁰:

$$\begin{aligned} F_{bulk} = & \alpha_1 \left(P_1^2 + P_2^2 + P_3^2 \right) + \alpha_{11} \left(P_1^4 + P_2^4 + P_3^4 \right) + \alpha_{12} \left(P_1^2 P_2^2 + P_2^2 P_3^2 + P_1^2 P_3^2 \right) \\ & + \alpha_{111} \left(P_1^6 + P_2^6 + P_3^6 \right) \\ & + \alpha_{112} \left[P_1^4 \left(P_2^2 + P_3^2 \right) + P_2^4 \left(P_1^2 + P_3^2 \right) + P_3^4 \left(P_1^2 + P_2^2 \right) \right] + \alpha_{123} P_1^2 P_2^2 P_3^2 \end{aligned}$$

where, α_i , α_{ij} , α_{ijk} represent the Landau parameters, which can be obtained experimentally. The elastic energy density is given by:

$$F_{elas} = C_{ijkl}(\varepsilon_{ij} - \varepsilon_{ij}^0)(\varepsilon_{kl} - \varepsilon_{kl}^0)$$

here, C_{ijkl} is the elastic stiffness tensor, ε_{ij} is the total strain, and ε_{ij}^0 is the spontaneous strain during the phase transformation. The spontaneous strain is related to the polarization through the electrostrictive coefficients, $\varepsilon_{ij}^0 = Q_{ijkl}P_kP_l$, where Q_{ijkl} is the electrostrictive coefficient. The anisotropy factor is defined as $A = C_{44}/C_{11}$. The gradient energy density is expressed as:

$$F_{grad} = G_{ijkl}P_{i,j}P_{k,l}$$

here, G_{ijkl} is the gradient coefficient, and $P_{i,j}$ denotes the derivative of the i th component of the polarization vector P_i with respect to the j th coordinate. In three-dimensional space, $i, j = 1, 2, 3$. The electrostatic field energy f_{elec} in this system can be expressed as:

$$f_{elec} = -E_i P_i - \frac{1}{2} \varepsilon_0 \kappa_{ij} E_i E_j$$

where, E_i represents the electric field component, ε_0 is the vacuum permittivity, and κ_{ij} is the dielectric constant.

The parameters are provided as follows: $\alpha_1 = 4.124 \times 10^5 (T - T_0)$, $\alpha_{11} = -5 \times 10^8 (c - c_0)$, $\alpha_{12} = 8.0 \times 10^8 (c - c_0) + 2\alpha_{11}$, $\alpha_{111} = 1.294 \times 10^9 (c - c_0)$, $\alpha_{112} = 1.5 \times 10^9 (c - c_0) + 3\alpha_{111}$, $\alpha_{113} = 7.5 \times 10^8 (c - c_0) + 6\alpha_{111}$, $Q_{11} = 0.1$, $Q_{12} = -0.034$, $Q_{44} = 0.029$, $s_{11} = 9.1 \times 10^{-12}$, $s_{12} = -3.2 \times 10^{-10}$, $s_{44} = 8.2 \times 10^{-10}$, $c = 0.06$. These parameters are all in SI units. The compliance coefficients are represented by 's', the Curie temperature is denoted by 'T₀', and the doping level and critical doping level are represented by 'c' and 'c₀', respectively. The simulation scale is 128dx×128dy×12dz, with grid scales dx, dy, and dz set to 1 nm. The thickness of the substrate and air layers is set to 2 nm. The semi-implicit Fourier-spectral method is used to solve the equations.

Reporting summary

Further information on research design is available in the Nature Portfolio Reporting Summary linked to this article.

Data availability

All the data supporting the findings of this study have been deposited in the Figshare database⁴¹ under accession code <https://doi.org/10.6084/m9.figshare.29555498>.

References

1. Devonshire, A. Theory of ferroelectrics. *Adv. Phys.* **3**, 85–130 (1954).
2. Scott, J. Applications of modern ferroelectrics. *Science* **315**, 954–959 (2007).
3. Béa, H. et al. Evidence for room-temperature multiferroicity in a compound with a giant axial ratio. *Phys. Rev. Lett.* **102**, 217603 (2009).
4. Mazumdar, D. et al. Nanoscale switching characteristics of nearly tetragonal BiFeO₃ thin films. *Nano Lett.* **10**, 2555–2561 (2010).
5. Zhang, J. et al. Microscopic origin of the giant ferroelectric polarization in tetragonal-like BiFeO₃. *Phys. Rev. Lett.* **107**, 147602 (2011).
6. Zhang, L. et al. Giant polarization in super-tetragonal thin films through interphase strain. *Science* **361**, 494–497 (2018).
7. Wang, Y. et al. Chemical-pressure-modulated BaTiO₃ thin films with large spontaneous polarization and high curie temperature. *J. Am. Chem. Soc.* **143**, 6491–6497 (2021).
8. Sun, Y. et al. Ultrahigh energy storage density in glassy ferroelectric thin films under low electric field. *Adv. Sci.* **9**, 2203926 (2022).
9. Huang, C. et al. A highly strained phase in PbZrO₃–2TiO₃–8O₃ films with enhanced ferroelectric properties. *Adv. Sci.* **8**, 2003582 (2021).
10. Boota, M. et al. Properties of epitaxial,(001)-and (110)-oriented (PbMg1/3Nb2/3O3) 2/3-(PbTiO3) 1/3 films on silicon described by polarization rotation. *Sci. Technol. Adv. Mater.* **17**, 45–57 (2016).
11. Cohen, R. E. Origin of ferroelectricity in perovskite oxides. *Nature* **358**, 136–138 (1992).
12. Miedema, P. S. & De Groot, F. M. The iron L edges: Fe 2p X-ray absorption and electron energy loss spectroscopy. *J. Electron. Spectrosc. Relat. Phenom.* **187**, 32–48 (2013).
13. Gholam, T. et al. Synchrotron X-ray Absorption Spectroscopy Study of Local Structure in Al-Doped BiFeO₃ Powders. *Nanoscale Res. Lett.* **14**, 1–12 (2019).
14. Luo, H. et al. Achieving giant electrostrain of above 1% in (Bi, Na) TiO₃-based lead-free piezoelectrics via introducing oxygen-defect composition. *Sci. Adv.* **9**, eade7078 (2023).
15. Mastelaro, V. R., Neves, P., Michalowicz, A. & Eiras, J. Electronic structure of Pb_{1-x}Ba_xZrO₃–65TiO₃–35O₃ ferroelectric compounds probed by soft x-ray absorption spectroscopy. *J. Phys.: Condens. Matter* **19**, 226212 (2007).
16. Zhang, W. et al. Tetragonal distortion of a BaTiO₃/BiO₃–5NaO₃–5TiO₃ nanocomposite responsible for anomalous piezoelectric and ferroelectric behaviors. *ACS omega* **5**, 22800–22807 (2020).
17. Wu, M. et al. Investigation of the multiplet features of SrTiO₃ in X-ray absorption spectra based on configuration interaction calculations. *J. Synchrotron Radiat.* **25**, 777–784 (2018).
18. Kim, J. H. et al. Defective ZnFe₂O₄ nanorods with oxygen vacancy for photoelectrochemical water splitting. *Nanoscale* **7**, 19144–19151 (2015).
19. Chang, H. et al. Effects of oxygen mobility in La–Fe-based perovskites on the catalytic activity and selectivity of methane oxidation. *ACS Catal.* **10**, 3707–3719 (2020).
20. Petralanda, U., Kruse, M., Simons, H. & Olsen, T. Oxygen vacancies nucleate charged domain walls in ferroelectrics. *Phys. Rev. Lett.* **127**, 117601 (2021).

21. Shibata, N. et al. Differential phase-contrast microscopy at atomic resolution. *Nat. Phys.* **8**, 611–615 (2012).
22. Meyer, K. C., Koch, L. & Albe, K. Phase transformations in the relaxor Na1/2Bi1/2TiO3 studied by means of density functional theory calculations. *J. Am. Ceram. Soc.* **101**, 472–482 (2018).
23. Wu, M. et al. Flexoelectric thin-film photodetectors. *Nano Lett.* **21**, 2946–2952 (2021).
24. Zubko, P., Catalan, G. & Tagantsev, A. K. Flexoelectric effect in solids. *Annu. Rev. Mater. Res.* **43**, 387–421 (2013).
25. Warren, W., Dimos, D., Tuttle, B., Nasby, R. & Pike, G. Electronic domain pinning in Pb (Zr, Ti) O3 thin films and its role in fatigue. *Appl. Phys. Lett.* **65**, 1018–1020 (1994).
26. Ong, S. P. et al. Python Materials Genomics (pymatgen): A robust, open-source python library for materials analysis. *Comput. Mater. Sci.* **68**, 314–319 (2013).
27. Perdew, J. P., Burke, K. & Ernzerhof, M. Generalized gradient approximation made simple. *Phys. Rev. Lett.* **77**, 3865 (1996).
28. Kresse, G. & Furthmüller, J. Efficient iterative schemes for ab initio total-energy calculations using a plane-wave basis set. *Phys. Rev. B* **54**, 11169 (1996).
29. Kresse, G. & Joubert, D. From ultrasoft pseudopotentials to the projector augmented-wave method. *Phys. Rev. B* **59**, 1758 (1999).
30. Blöchl, P. E. Projector augmented-wave method. *Phys. Rev. B* **50**, 17953 (1994).
31. Cazorla, C. & Stengel, M. Ab initio design of charge-mismatched ferroelectric superlattices. *Phys. Rev. B* **90**, 020101 (2014).
32. Cazorla, C. & Stengel, M. Electrostatic engineering of strained ferroelectric perovskites from first principles. *Phys. Rev. B* **92**, 214108 (2015).
33. Cazorla, C. & Íñiguez, J. Insights into the phase diagram of bismuth ferrite from quasiharmonic free-energy calculations. *Phys. Rev. B* **88**, 214430 (2013).
34. Cazorla, C., Diéguez, O. & Íñiguez, J. Multiple structural transitions driven by spin-phonon couplings in a perovskite oxide. *Sci. Adv.* **3**, e1700288 (2017).
35. Menéndez, C., Chu, D. & Cazorla, C. Oxygen-vacancy induced magnetic phase transitions in multiferroic thin films. *NPJ Comput. Mater.* **6**, 76 (2020).
36. Menéndez, C. & Cazorla, C. Giant Thermal Enhancement of the Electric Polarization in Ferrimagnetic BiFe1-x Co x O 3 Solid Solutions near Room Temperature. *Phys. Rev. Lett.* **125**, 117601 (2020).
37. Chen, L. Q. Phase-field method of phase transitions/domain structures in ferroelectric thin films: a review. *J. Am. Ceram. Soc.* **91**, 1835–1844 (2008).
38. Li, Y., Hu, S., Liu, Z. & Chen, L. Phase-field model of domain structures in ferroelectric thin films. *Appl. Phys. Lett.* **78**, 3878–3880 (2001).
39. Wang, J., Shi, S.-Q., Chen, L.-Q., Li, Y. & Zhang, T.-Y. Phase-field simulations of ferroelectric/ferroelastic polarization switching. *Acta Mater.* **52**, 749–764 (2004).
40. Liu, D. et al. Phase-field simulations of vortex chirality manipulation in ferroelectric thin films. *npj Quantum Mater.* **7**, 34 (2022).
41. Sun, Y. et al. Flexoelectricity-driven giant polarization in (Bi, Na) TiO3-based ferroelectric thin films. figshare. Dataset. <https://doi.org/10.6084/m9.figshare.29555498>. (2025).
42. Wu, J., Qiao, S., Wang, J., Xiao, D. & Zhu, J. A giant polarization value of Zn and Mn co-modified bismuth ferrite thin films. *Appl. Phys. Lett.* **102**, (2013).
43. Wu, J. & Wang, J. Bilayered BiFe0.95Mn0.05O3/Bi0.90La0.10FeO3 thin films with low ferroelectric coercivity and large remanent polarization. *J. Am. Ceram. Soc.* **93**, 2113–2116 (2010).
44. Morioka, H., Asano, G., Oikawa, T., Funakubo, H. & Saito, K. Large remanent polarization of 100% polar-axis-oriented epitaxial tetragonal Pb (Zr0.35 Ti0.65) O3 thin films. *Appl. Phys. Lett.* **82**, 4761–4763 (2003).
45. Khan, M. A., Comyn, T. P. & Bell, A. J. Large remanent polarization in ferroelectric BiFeO3–PbTiO3 thin films on Pt/ Si substrates. *Appl. Phys. Lett.* **91**, (2007).

Acknowledgements

The financial support of the Australian Research Council (FT180100541, DP220103229, DP250100778). This work is supported by the National Natural Science Foundation of China (52372100). Z.C acknowledge the support of the National Natural Science Youth Foundation of China (Grant No. 12204393), the Research Grant Council of Hong Kong Special Administrative Region China (Project No. PolyU25300022), and the GuangDong Basic and Applied Basic Research Foundation of the Department of Science and Technology of Guangdong Province (Grant No. 2024A1515012752). C.C. acknowledges support from the Spanish Ministry of Science, Innovation, and Universities under the “Ramón y Cajal” fellowship RYC2018-024947-I and TED2021-130265B-C22. Computational resources and technical assistance were provided by the Red Española de Supercomputación (RES) under the grants FI2023-1-0002, FI-2023-2-0004, and FI-2022-3-0014. J.Y. acknowledge the support for computational resource from the National Computing Infrastructure on the Gadi supercomputer under the project dy3, as well as the financial support from the Materials and Manufacturing Futures Institute, UNSW. This work was performed in part at the New South Wales node of the Australian National Fabrication Facility, a company established under the National Collaborative Research Infrastructure Strategy to provide nano and microfabrication facilities for Australia’s researchers. The authors also acknowledge the facilities and the scientific and technical assistance of the Microscopy Australia node at the University of Sydney (Sydney Microscopy & Microanalysis) and Electron Microscope Unit (EMU), Mark Wainwright Analytical Centre at the University of New South Wales.

Author contributions

Y.S. conducted the majority of the experiments, performed data analysis, and drafted the manuscript. R.N. carried out the STEM experiments, while Z.S., S.C., and Z.C. analyzed the corresponding results. S.T., C.G., and H.H. performed the phase-field simulations. H.W., X.G., and J.Z. conducted the XAS experiments, whereas J.Y. and C.C. carried out the DFT simulations. X.L. and S.Z. contributed to manuscript revisions. D.W. supervised the project, conceived the research concept, designed the experiments, and provided critical revisions to the manuscript.

Competing interests

The authors declare no competing interests.

Additional information

Supplementary information The online version contains supplementary material available at <https://doi.org/10.1038/s41467-025-65610-5>.

Correspondence and requests for materials should be addressed to Houbing Huang, Zibin Chen or Danyang Wang.

Peer review information *Nature Communications* thanks Eunmi Lee, Alexander Tselev and the other anonymous reviewer(s) for their contribution to the peer review of this work. A peer review file is available.

Reprints and permissions information is available at <http://www.nature.com/reprints>

Publisher's note Springer Nature remains neutral with regard to jurisdictional claims in published maps and institutional affiliations.

Open Access This article is licensed under a Creative Commons Attribution-NonCommercial-NoDerivatives 4.0 International License, which permits any non-commercial use, sharing, distribution and reproduction in any medium or format, as long as you give appropriate credit to the original author(s) and the source, provide a link to the Creative Commons licence, and indicate if you modified the licensed material. You do not have permission under this licence to share adapted material derived from this article or parts of it. The images or other third party material in this article are included in the article's Creative Commons licence, unless indicated otherwise in a credit line to the material. If material is not included in the article's Creative Commons licence and your intended use is not permitted by statutory regulation or exceeds the permitted use, you will need to obtain permission directly from the copyright holder. To view a copy of this licence, visit <http://creativecommons.org/licenses/by-nc-nd/4.0/>.

© The Author(s) 2025

¹School of Materials Science and Engineering, The University of New South Wales, Sydney, Australia. ²Australian Centre for Microscopy and Microanalysis, The University of Sydney, Sydney, Australia. ³School of Aerospace, Mechanical and Mechatronic Engineering, The University of Sydney, Sydney, Australia. ⁴State Key Laboratory of Ultra-Precision Machining Technology, Department of Industrial and Systems Engineering, The Hong Kong Polytechnic University, Kowloon, Hong Kong, China. ⁵Research Institute for Advanced Manufacturing, Department of Industrial and Systems Engineering, The Hong Kong Polytechnic University, Hong Kong, China. ⁶Advanced Research Institute of Multidisciplinary Science, Beijing Institute of Technology, Beijing, China. ⁷Global Innovative Center for Advanced Nanomaterials, College of Engineering, Science and Environment, The University of Newcastle, Callaghan, New South Wales, Australia. ⁸Materials and Manufacturing Futures Institute, The University of New South Wales, Sydney, Australia. ⁹Departament de Física, Universitat Politècnica de Catalunya, Barcelona, Spain. ¹⁰Frontier Institute of Science and Technology, State Key Laboratory for Mechanical Behavior of Materials and Future Industrial Innovation Institute of Emerging Information Storage and Smart Sensor, Xi'an Jiaotong University, Xi'an, China. ¹¹Department of Chemistry, City University of Hong Kong, Hong Kong, China.  e-mail: hbhuang@bit.edu.cn; zi-bin.chen@polyu.edu.hk; dy.wang@unsw.edu.au